Saharan Dust Aerosol Radiative Forcing Measured from Space

F. LI

Center for Atmospheric Sciences, Scripps Institution of Oceanography, University of California, San Diego, La Jolla, California

A. M. VOGELMANN

Earth Systems Science Division, Brookhaven National Laboratory, Upton, New York

V. RAMANATHAN

Center for Atmospheric Sciences, Scripps Institution of Oceanography, University of California, San Diego, La Jolla, California

ABSTRACT

This study uses data collected from the Clouds and the Earth's Radiant Energy System (CERES) and the Moderate Resolution Imaging Spectroradiometer (MODIS) instruments to determine Saharan dust broadband shortwave aerosol radiative forcing over the Atlantic Ocean near the African coast (15°–25°N, 45°–15°W). The clear-sky aerosol forcing is derived directly from these data, without requiring detailed information about the aerosol properties that are not routinely observed such as chemical composition, microphysical properties, and their height variations. To determine the diurnally averaged Saharan dust radiative forcing efficiency (i.e., broadband shortwave forcing per unit optical depth at 550 nm, $W m^{-2} \tau_a^{-1}$), two extreme seasons are juxtaposed: the high-dust months [June–August (JJA)] and the low-dust months [November–January (NDJ)]. It is found that the top-of-atmosphere (TOA) diurnal mean forcing efficiency is $-35 \pm 3 \ W m^{-2} \tau_a^{-1}$ for JJA, and $-26 \pm 3 \ W m^{-2} \tau_a^{-1}$ for NDJ. These efficiencies can be fit by reducing the spectrally varying aerosol single-scattering albedo such that its value at 550 nm is reduced from 0.95 ± 0.04 for JJA to about 0.86 ± 0.04 for NDJ. The lower value for the low-dust months might be influenced by biomass-burning aerosols that were transported into the study region from equatorial Africa. Although the high-dust season has a greater (absolute value of the) TOA forcing efficiency, the low-dust season may have a greater surface forcing efficiency. Extrapolations based on model calculations suggest the surface forcing efficiencies to be about $-65 \ W m^{-2} \tau_a^{-1}$ for the high-dust season versus $-81 \ W m^{-2} \tau_a^{-1}$ for the low-dust season. These observations indicate that the aerosol character within a region can be readily modified, even immediately adjacent to a powerful source region such as the Sahara. This study provides important observational constraints for models of dust radiative forcing.

1. Introduction

In the Sahara and bordering regions, aeolian processes mobilize and suspend considerable quantities of aerosols in the atmosphere. Of the total global production, estimates of which vary between 1000 and 3000 Tg yr^{-1} (Andreae 1995; Duce 1995), more than half generally originates over West Africa (Mbourou et al. 1997). Much attention has been paid to the Saharan dust radiative forcing during the recent decade. Observational analyses have been based on in situ ground or airborne measurements (Li et al. 1996; Fouquart et al. 1987; Quijano et al. 2000; Haywood et al. 2001), surface radiometer measurements (Diaz et al. 2001; Dubovik et al. 2002), dust transport models and satellite observations (Weaver et al. 2002), and combined satellite measurements of aerosol loading and top-of-atmosphere (TOA) broadband fluxes (Hsu et al. 2000; Loeb and Kato 2002; Christopher and Zhang 2002).

Here we examine the seasonal dependence of the Saharan dust aerosol radiative forcing over the Atlantic Ocean near the African coast (15°–25°N, 45°–15°W) using satellite data from the Clouds and the Earth's Radiant Energy System (CERES) and the Moderate Resolution Imaging Spectroradiometer (MODIS). While previous studies have explored the aerosol radiative forcing for a specific period, we seek to explicitly explore its seasonal variation by contrasting two seasons: a high-dust period from June–August (JJA), and a low-dust period from November–January (NDJ). We will show that aerosol character can undergo a profound seasonal change that affects the aerosol radiative forcing. We approach this question by deriving the clear-sky dust aerosol forcing directly from these data. Thus we do

Corresponding author address: Dr. Fang Li, Center for Atmospheric Sciences, Scripps Institution of Oceanography, UCSD, 9500 Gilman Drive, Mail Code 0221, La Jolla, CA 92093-0221.
E-mail: fli@fiji.ucsd.edu

not require detailed information about aerosol properties that are not routinely observed, such as chemical composition, microphysical properties, and their height variations. This is achieved by correlating the aerosol optical depth estimate from MODIS with broadband fluxes from CERES on a pixel-to-pixel basis for each solar zenith angle. The regression slope thus obtained is the TOA aerosol forcing efficiency (radiative forcing per unit aerosol optical depth). Additionally, this information with the constraints of MODIS effective radii enables diagnosing the effective aerosol single-scattering albedo that would match this forcing efficiency. By applying this single-scattering albedo to a model, we can estimate the forcing efficiency at the surface. These data will provide useful information to diagnose the effects of the aerosol on the regional-scale energy balance.

In section 2, we describe the criteria for choosing CERES and MODIS data used in this study. In section 3, we discuss the regression approach for obtaining the forcing efficiency and the results. We discuss sources of uncertainty in section 4, and conclusions in section 5.

2. Data

The Earth Observing System *Terra* satellite was launched on 18 December 1999. It is a multi-instrument platform that carries the MODIS and CERES sensors. *Terra* has a sun-synchronous orbit with the orbit period of 98 min, and a ground-track repeat cycle of 16 days.

MODIS (Kaufman et al. 2000) has a viewing swath width of 2330 km, and views the entire surface of Earth in 36 spectral bands (0.4–14 μm). MODIS aerosol products have undergone a rapid update since their first release in August 2000. The current version 3 provides nearly global coverage starting November 2000. For this study, we used a 14-month series of the version 3 products spanning a period from November 2000 to December 2001. We use the MODIS level 2-v3 products (MOD04_L2) that have a 10-km spatial resolution at nadir. The parameters used include the 550-nm wavelength aerosol optical depth (AOD) over ocean, aerosol effective radius, solar zenith angle, and scattering angle.

CERES has three channels: a shortwave channel to measure reflected sunlight, a longwave channel to measure Earth-emitted thermal radiation in the 8–12-μm "window" region, and a total channel to measure all wavelengths of radiation (Wielicki et al. 1996). The resolution of CERES-Terra is 20 km at nadir. To examine TOA shortwave flux, we use the CERES (Earth Radiation Budget Experiment) ERBE-like Science Product (ES8) dataset. The ES8 parameters used are the TOA shortwave flux (wavelength range 0.3–5.0 μm), the solar zenith angle, and the scene type. We only use clear-sky measurements over the ocean ("clear ocean" scene type).

a. Solar zenith screening

Estimates of instantaneous aerosol radiative forcing are quite sensitive to the solar zenith angle (Rajeev and Ramanathan 2001; Haywood et al. 2001; Loeb and Kato 2002). We first examine the consistency of the solar zenith angles recorded by the MODIS and CERES instruments. The measurements are collocated at a $0.2° \times 0.2°$ grid for a test region from 90°N to 90°S and 90°W to 90°E using a method similar to Rajeev and Ramanathan (2001). The CERES and MODIS data located within each grid are binned. The CERES 20-km resolution is already equivalent to 0.2° at the central latitude of the test region. MODIS data has the equivalent resolution of 0.1° and multiple measurements within each 0.2° bin are averaged. We apply an additional constraint that the MODIS and CERES solar zenith angles must agree within 0.5°, which removes approximately 4% of the points.

b. MODIS AOD

Our study region is over the Atlantic Ocean northwest of the Sahara (15°–25°N, 45°–15°W). Figure 1 shows the MODIS AOD (550 nm) distributions over the target area for two extreme cases: during a high-dust month (July 2001), and a low-dust month (December 2000). The AOD values in Fig. 1 are the average of all the observations per month within each $0.2° \times 0.2°$ grid over the oceanic regions within our study region. In July (Fig. 1a), dense dust plumes stream out of the northwestern Africa coastal region, with AOD even reaching 1.0. The dust plumes spread westerly toward the remote Atlantic. By contrast in December (Fig. 1b), the AOD in the study area dwindles to 0.15.

Atmospheric circulation and aerosol lifetime are critical factors that control the distribution and transport of aerosols over the ocean. The dust transport is significantly dominated by the prevailing wind in the low troposphere (Li and Ramanathan 2002). Figure 2 gives a seasonal mean wind field in the 700-mb layer for two periods: JJA, and NDJ. During JJA a strong easterly wind is driven by differential heating between land areas in the Saharan desert and adjacent ocean areas; the highest wind speed is up to 12 m s^{-1}. In NDJ, however, the wind speed decreases to about 2 m s^{-1} in the study region, which limits the dust transport. [Data are from the National Centers for Environmental Prediction–National Center for Atmospheric Research (NCEP–NCAR) reanalysis available from the National Oceanic and Atmospheric Administration–Cooperative Institute for Research in Environmental Sciences (NOAA–CIRES) Climate Diagnostics Center.]

The annual variation of the MODIS AOD within the study region is shown in Fig. 3 on a monthly mean basis. (The monthly average is determined from the daily regional averages, where each regional average is determined from an average of the 0.2° binned data.) A
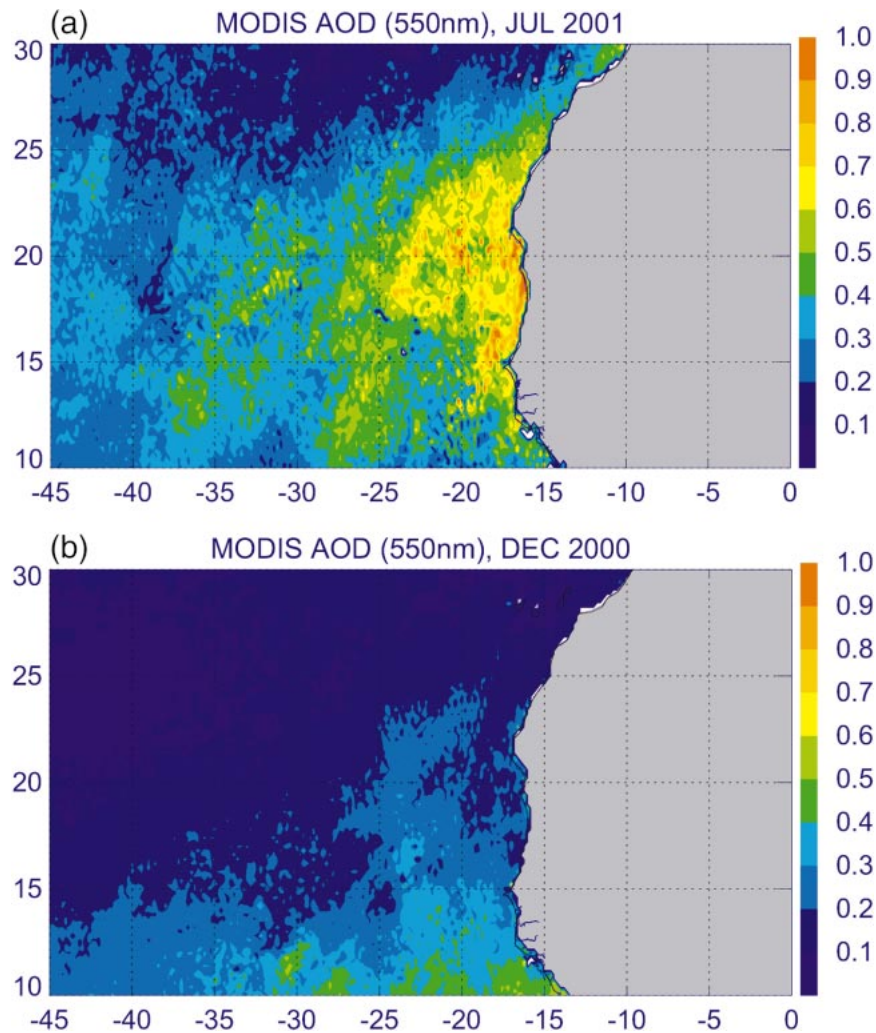
FIG. 1. MODIS aerosol plumes for our study region in (a) Jul 2001 and (b) Dec 2000. The aerosol optical depth at 550 nm is given by the color scale at the right.

clear seasonal cycle is seen with heavy dust events during JJA, and a low aerosol loading in NDJ. Even though the aerosol loading is less in NDJ, the AOD over the study area is still as large as 0.15, which is 3 times higher than the average value (0.05) expected over the remote North Atlantic area (Husar et al. 1997). This suggests that African aerosols affect the region in any season. In February, a secondary AOD peak is found that reaches 0.4. It is not an occasional episode, as the February plume has captured attention for years (Husar et al. 1997; Ellis and Merrill 1995; Li et al. 1996). The AOD and wind flow in February 2001 are illustrated in Fig. 4, which show that the northward spread of the aerosol plumes basically follows the wind speed gradient. This suggests that the second aerosol plume is linked to the periodic African biomass burning events, given by the MODIS fire detection product (available online at http://rapidfire.sci.gsfc.nasa.gov/products_rr. html).

c. MODIS aerosol effective radius

Scattering and absorption by airborne particles strongly depend on their size. Effective radius, r_{eff}, is used to quantify, in a single value, the size of a polydispersed particle size distribution. The effective radius is the surface-weighted size of equivalent spherical particles, which is a measure of the total volume to the surface area for a distribution of aerosol particles (Hess et al. 1998). MODIS provides an estimate of the aerosol effective radii, which will be used to constrain the diurnal flux integration and estimate the single-scattering albedo. Uncertainties in the MODIS effective radii and their effects on the analyses are discussed in section 4.

Figure 5 shows the frequency distributions of the MODIS effective radii for the dust seasons (JJA and NDJ). The number of observations during JJA is less than NDJ because more cloudy days occur during the
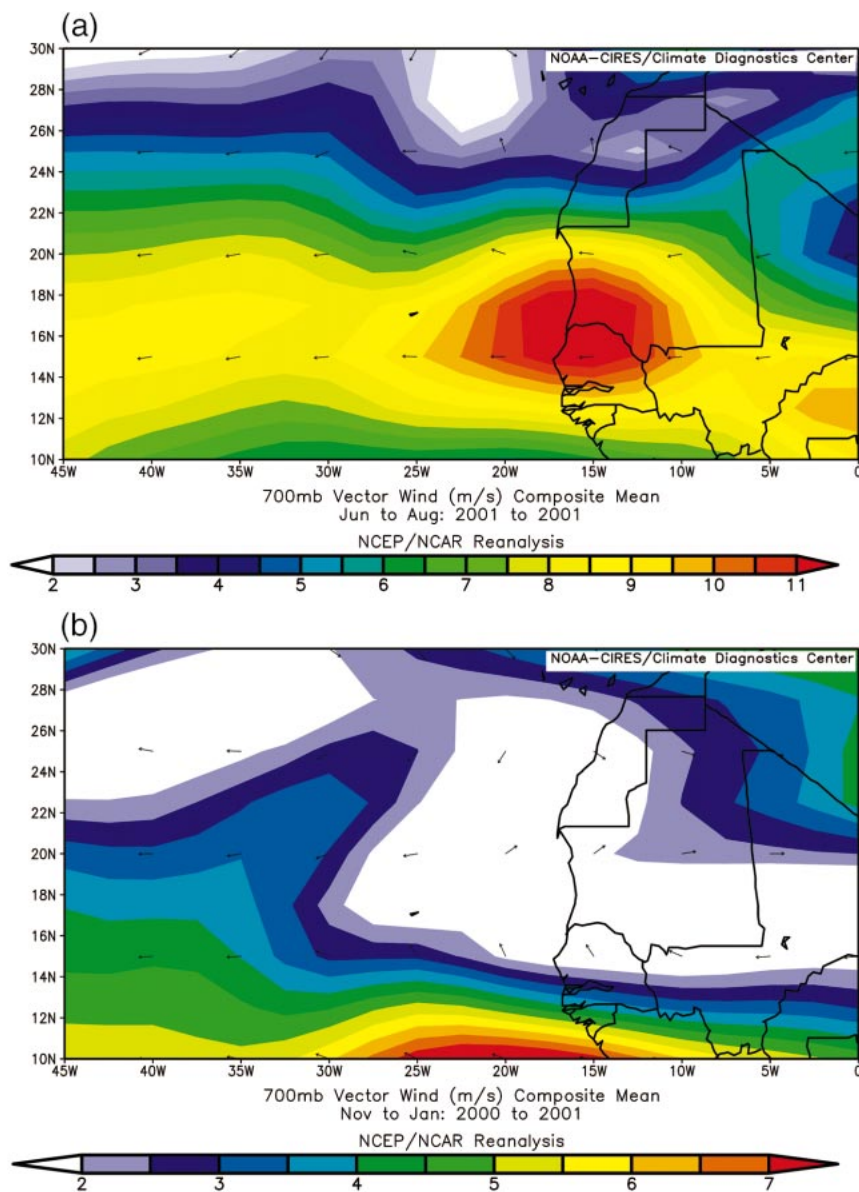
FIG. 2. Mean wind field (m s^{-1}) at 700 mb for (a) the high-dust season months (JJA), and (b) the low-dust season (NDJ). Arrows indicate the wind vector, and the color indicates the wind speed.

warmer season. For NDJ, the effective radii are all concentrated around 0.55 μm. The distributions during JJA are much broader than for NDJ, and the average effective radii for July and August increase by about 0.35 μm to about 0.9 μm. June has a mode that is more similar to the NDJ period than to neighboring months July and August. The reason for this dissimilarity is uncertain, but might be related to June being a transition month when the aerosol properties are undergoing a seasonal shift. Note, for example, that the largest standard deviations in AOD occurred during June (Fig. 3).

3. Methodology

a. Aerosol forcing efficiency

The top-of-atmosphere (TOA) direct radiative forcing (ΔF) of aerosols for cloud-free sky is defined as

$$\Delta F = F_{na} - F_a, \tag{1}$$

where F_{na} is the broadband shortwave (SW) flux in the absence of aerosols, and F_a is the flux in the presence of aerosols. The aerosol forcing efficiency (f_e) is the radiative forcing produced by a unit of AOD (W m^{-2} τ_a^{-1}). Many prior studies have determined ΔF by modeling the aerosol-
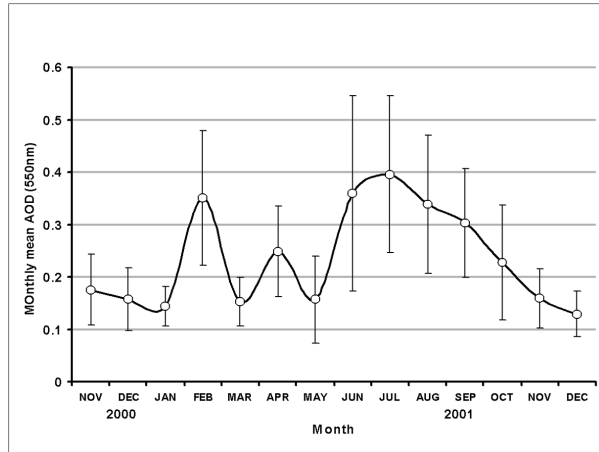
FIG. 3. Seasonal variation of the MODIS monthly mean AOD (550 nm) in our study region, the northwest of Africa (15°–25°N, 45°–15°W) from Nov 2000 to Dec 2001. Vertical bars for each month indicate one standard deviation of the daily variability.

free flux, F_{na}. However, such an approach assumes that the model will reproduce the aerosol-free flux as seen by the instrument when in fact there may be modeling or instrumental offsets (Satheesh and Ramanathan 2000; Conant 2000). We avoid modeling F_{na} by taking the derivative of the expression (1) with respect to a narrowband AOD, τ_a, to get the instantaneous efficiency $f_e(\theta)$ as (Rajeev and Ramanathan 2001)

$$f_e(\theta) = d(\Delta F)/d\tau_a = -dF_a/d\tau_a. \quad (2)$$

Thus by treating the efficiency (i.e., the slope), biases are removed from the analysis. The instantaneous forcing efficiency is a function of the solar zenith angle, and the next section describes how we obtain it from the MODIS data. Section 3c explains how instantaneous forcing efficiencies are used to compute diurnally averaged forcing efficiencies that are more relevant to climate studies of the earth's energy balance.

Note that following the convention of earlier studies (e.g., Satheesh and Ramanathan 2000; Conant 2000; Rajeev and Ramanathan 2001) the forcing efficiency is defined as the derivative of the broadband shortwave flux with respect to a narrowband AOD (in our case, at 550 nm). It might seem more consistent to use a broadband, spectrally averaged AOD to evaluate the derivative of the broadband flux; however, sufficient multispectral AODs are not available to provide a shortwave broadband average. Aerosol spectral AODs tend, in general, to be broad and smoothly varying (especially for large dust particles); thus, it is reasonable to use the value at 550 nm as an "index" because of the large amount of shortwave energy incident at (or near) this wavelength, and the corresponding effect of this energy on the broadband CERES flux.

b. Slope determination

The value F_a is represented by the instantaneous CERES TOA fluxes, which are collocated with, τ_a, the MODIS AOD at 550 nm. For convenience, F_a is converted into TOA albedo by dividing by the TOA instantaneous solar flux incident at each pixel location. Figure 6 shows scatterplots of clear-sky CERES SW albedos versus τ_a for our study region in July 2001 (a high-dust month) and November 2000 (a low-dust month). Because TOA albedo depends strongly on the solar zenith angle, the solar zenith angles for each plot are limited to be within a 5° interval: 20°–25° for July, and 40°–45° for November (for this illustration, different ranges are used per month to adjust for the difference in solar declination angle in order to show the typical patterns per season). The relative large scatter seen in Fig. 6 is due to the uncertainties in the models used to convert radiances to TOA albedo, cloud contamination, and other factors discussed in section 4.

To obtain the instantaneous slope of albedo in terms of τ_a for each solar zenith angle bin, three fitting procedures were tested. The first procedure is linear-direct fitting, where a linear regression is performed on all of the points (the line in Fig. 6). The second procedure is binned-mean fitting: the TOA albedos are binned by narrow AOD intervals (0.02), an average albedo is computed for each bin, and a linear fit is performed on the averages (solid squares). The third procedure is binned-minimum fitting: for each narrow AOD interval, only the minimum TOA albedo for each bin is used (solid triangles). Both binning procedures require a minimum of 200 points to create a bin. (The AOD axis stops at 0.5 in Fig. 6a and at 0.25 in Fig. 6b because there are not enough points within the 0.02 AOD intervals beyond those points that meet this criterion; however, the linear-direct fitting uses all points including those beyond the axes cutoffs.) As can be seen in Fig. 6, the three approaches produce similar slopes. As the solar zenith angle increases, more of the radiation is scattered into the upward hemisphere and, hence, enhances the slope (forcing) (Hignett et al. 1999; Loeb and Kato 2002; Haywood et al. 2001). We find that the linear-direct fitting follows this behavior the best of the three, with slopes that increase nearly monotonically with solar zenith angle (i.e., the slopes are least affected by scatter within the data). The binned-mean fitting is only −2.3% different on average from the linear-direct fitting. The binned-minimum fitting is most susceptible to scatter and differs from the linear-direct fitting on average by 13%. Therefore, we use the linear-direct fitting approach to derive the forcing efficiency in this study.

c. Diurnal average forcing efficiency

Figure 7 shows the albedo slopes versus solar zenith angle as obtained from the direct fitting procedure for the low-dust months (November and December 2000,
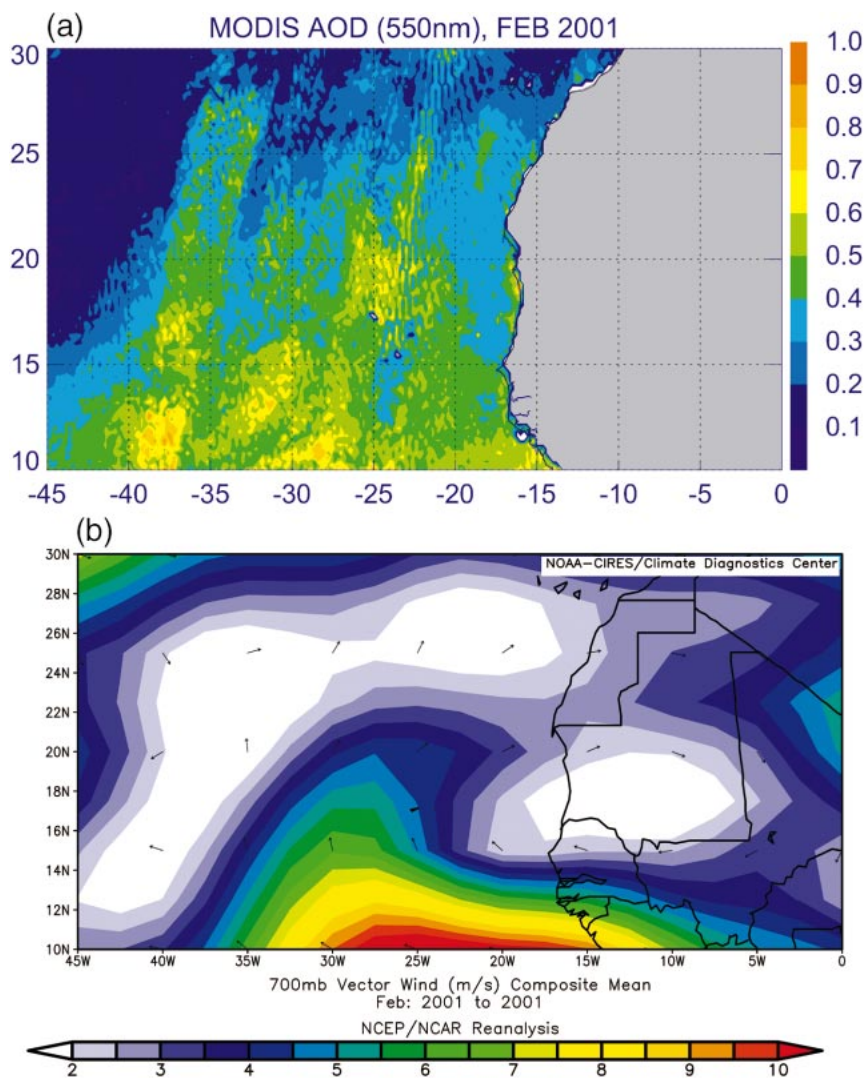
FIG. 4. Illustration of the northward aerosol invasion upon the study area coming from the biomass-burning regions in Feb 2001. (a) MODIS aerosol optical depth (550 nm) distribution, and (b) the 700-mb wind flow pattern from the NCEP–NCAR reanalysis; arrows indicate the wind vector, and the color indicates the wind speed.

and January 2001), and the high-dust months (June, July, and August 2001). The uncertainty in the slopes fitted by the linear-direct method (e.g., Fig. 6) are provided at each point by an error bar. (The average correlation coefficients of the albedo–AOD relationships are around 0.62 for NDJ and JJA, with values mostly ranging between 0.5 and 0.75 for both seasons and a minimum and maximum of 0.35 and 0.78.) Because the range of AOD is less for the NDJ low-dust months than for JJA, the scatter may cause a greater uncertainty in the slope fitting for NDJ. As can be seen, *Terra*'s sun-synchronous orbit limits the solar zenith angles available within our study region. The solar declination angle decreases in the latter part of the year and broadens the range of solar zenith angles for NDJ, but still not sufficiently to span the full range needed to evaluate the

diurnal average forcing efficiency. Thus, we employ a fitting procedure that is constrained by these observations in order to obtain values for the full range of solar zenith angles that are needed to evaluate the diurnal average forcing efficiency.

The fitting procedure uses calculations by the Santa Barbara discrete ordinate radiative transfer (DISORT) Atmospheric Radiative Transfer (SBDART) program (Ricchiazzi et al. 1998), which allows setting the spectral aerosol optical properties such as the extinction coefficient, single-scattering albedo, and asymmetry factor. The vertical distribution is specified in terms of an aerosol density profile (Hess et al. 1998) that decreases exponentially from 0 to 6 km by a scale height of 2 km, from 6 to 12 km by a scale height of 8 km, and from 12 to 35 km by a scale height of 99 km. The units used
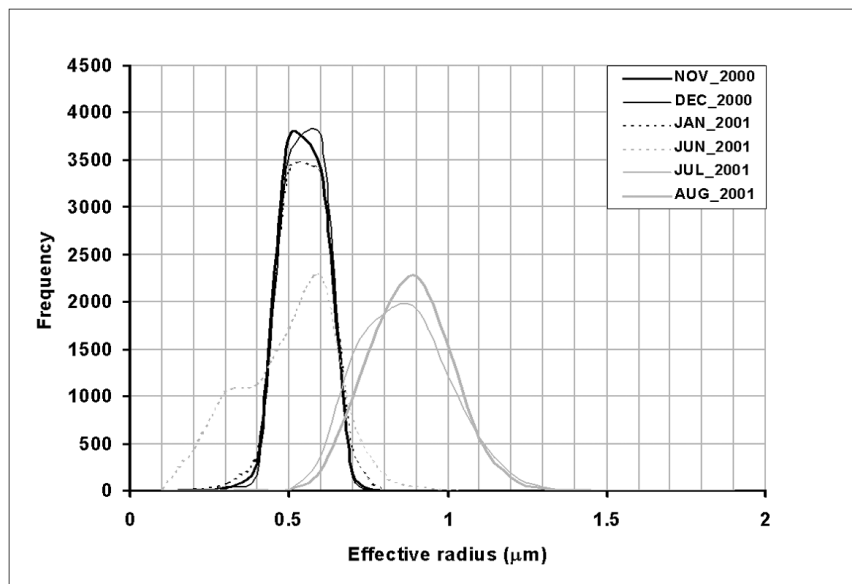
FIG. 5. Frequency distributions of MODIS aerosol effective radii within our study region for months NDJ and JJA.

to specify the aerosol density are arbitrary, since the overall profile is scaled by the user-specified total vertical optical depth (Ricchiazzi et al. 1998). The spectral aerosol optical properties are generated using the Optical Properties of Aerosols and Clouds (OPAC) model (Hess et al. 1998) from which we adopt the OPAC size distribution and refractive index for each component. The OPAC refractive indices of the aerosol components are mostly from d'Almeida et al. (1991), which partly refer to Shettle and Fenn (1979), and are corrected with respect to different sources in a few cases (Koepke et al. 1997). The size distributions are modeled using lognormal distributions that are a function of R_{mod} and σ. The OPAC aerosol types used and their R_{mod} and σ are (μm): water soluble (0.0306, 2.24), sea salt accumulation mode (0.416, 2.03), sea salt coarse mode (3.49, 2.03), mineral accumulation mode (0.39, 2.0), mineral coarse mode (1.90, 2.15), mineral transported (0.50, 2.2), and soot (0.0118, 2.00). The R_{mod} for the water soluble and sea salt components have a slight relative humidity dependence, and the values provided here are at 80% RH. The surface relative humidity is obtained from the NCEP–NCAR reanalyses (75% for NDJ and 80% for JJA), and the SBDART "tropical" atmospheric profile is used above that. (For additional aerosol information on the OPAC aerosol properties, see Hess et al. 1998).

A series of candidate aerosol models are constructed by systematically changing the mixing ratios of the aerosol types, while requiring that the resulting aerosol effective radius match the MODIS retrieval for each period. The effective radius constraint for each season is the average of its three monthly modes given in Fig. 5. For JJA the concentrations of the mineral dust, water-

soluble and sea salt components were varied, and soot needed to be included for NDJ in order to match the slopes. The component compositions for each of the models in terms of mixing ratio are, respectively for JJA and NDJ, 63%–49% for the mineral component, 8%–15% for the water soluble, and 29%–34% for the sea salt. Soot was included for NDJ at 2%. The mixing ratios of the aerosol components are kept constant with height. These models are used in SBDART, via optical depth in increments of 0.1 from 0.0 to 1.0, to generate d(albedo)/$d\tau_a$ curves that are compared to the observations. The constraints applied to the aerosol model fitting are stringent in that the simulated slopes must match the absolute magnitude (vertical offset in the curves), their variation with solar zenith angle, and match the MODIS-retrieved effective radius. The model that best fits the magnitude (offset) and solar zenith angle variation of the observed d(albedo)/$d\tau_a$ is selected for each season, based on the minimum rms between the observations and calculations. (Assumptions and uncertainties in the aerosol modeling are discussed in section 4.)

The models providing the best fits for the JJA and NDJ periods are shown in Fig. 7. The associated single-scattering albedos at 550 nm are, respectively, 0.95 ± 0.04 and 0.86 ± 0.04. The uncertainties are determined from the local derivative in forcing efficiency with respect to single-scattering albedo obtained from our aerosol models, attributing all of the uncertainty in forcing efficiency to that in the single-scattering albedo (which thus represents an upper limit). For comparison, we also plot the results for the OPAC oceanic aerosol model. Clearly, the conservative scattering ($\omega_0 = 1.0$) of the oceanic aerosols generates slopes that are much higher
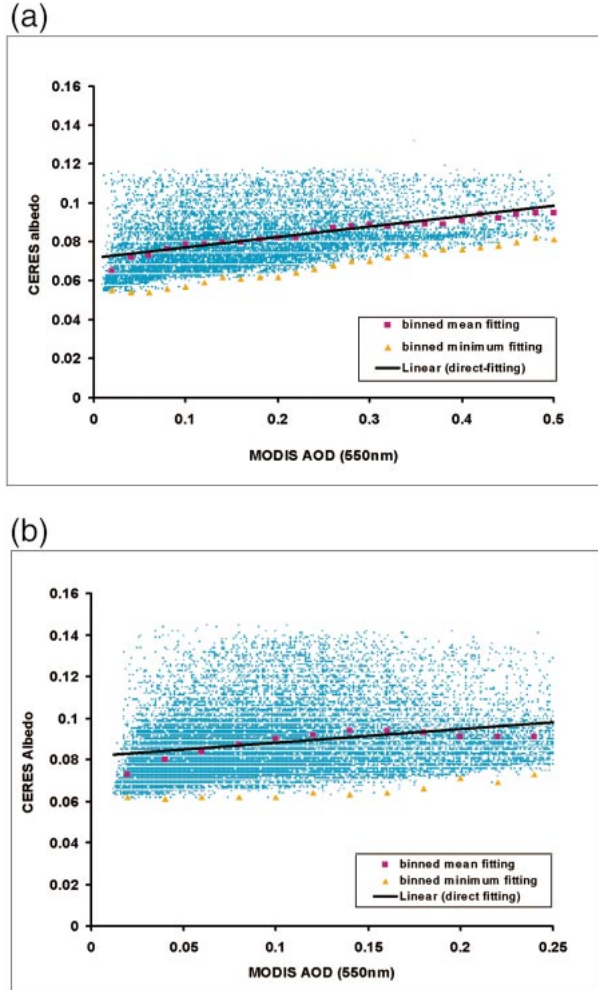
FIG. 6. Scatterplot of the CERES clear-sky TOA albedo and the collocated MODIS aerosol optical depth over ocean for our study region. The three fitting approaches used (indicated in the legend) are described in the text. (a) Jul 2001 for solar zenith angles 20°–25°. Total number of collocated points is 9915. (b) Nov 2000 for solar zenith angles 40°–45°. Total number of collocated points is 19 008.

than the other curves, providing a poor match to the observations.

The d(albedo)/$d\tau_a$ curves are integrated to obtain the diurnal average forcing efficiency, f_e, using (Rajeev and Ramanathan 2001),

$$ f_e = \frac{S_0}{2\pi}\left(\frac{d_0}{d}\right)^2 \int_{-h_0}^{h_0} \cos(\theta)\left[\frac{d(\text{albedo})}{d\tau_a}\right] d\theta, \quad (3) $$

where S_0 (=1367 W m^{-2}) is the mean solar flux per unit area at nadir for the mean Earth–Sun distance (d_0), d is the earth–sun distance for the given day of year, and h_0 is the hour angle at sunrise and sunset. For this integration, the mean solar geometry used is from 15 July for JJA, and 15 December for NDJ.

We find the TOA diurnal forcing efficiency to be -35

$\pm$ 3 W m^{-2} τ_a^{-1} for JJA, which reduces to -26 ± 3 W m^{-2} τ_a^{-1} for NDJ. The uncertainties are derived from the standard deviation of the best-fit curve around the observed points (8% and 13%, respectively, for JJA and NDJ). The seasonal mean aerosol optical depths are, respectively, 0.36 $\pm$ 0.16, and 0.16 $\pm$ 0.06. Thus, the corresponding diurnal mean TOA aerosol forcing averaged over the 3-month seasons are -12.6 ± 6 W m^{-2} for JJA and -4.2 ± 2 W m^{-2} for NDJ. Although the absolute magnitude of TOA forcing efficiency for JJA is larger than for NDJ, the greater atmospheric absorption (lower single-scattering albedo) for NDJ translates into it having a greater impact on the surface forcing efficiency. Our model estimates that the absolute magnitude of the surface forcing efficiency increases from -65 W m^{-2} τ_a^{-1} for the high-dust season (JJA) to -81 W m^{-2} τ_a^{-1} for the low-dust season (NDJ), or a 25% enhancement. These estimates of the surface forcing efficiency depend on model assumptions such as the aerosol height and, thus, involve more uncertainty than the TOA forcing efficiencies that are constrained directly by TOA measurements. However, assuming that such factors are similar between the two seasons, the relative difference in the surface forcing efficiencies for the JJA and NDJ periods should be captured by our estimates. This would suggest that the surface forcing for the two seasons could be similar, since the difference in seasonal surface forcing efficiencies would be partially compensated by the opposing differences in magnitudes of the seasonal average AODs.

d. Comparison with literature

The spectral variation of the aerosol single-scattering albedos estimated from the models for the JJA and NDJ seasons are shown in Fig. 8, which are compared to values from the literature. (For a discussion of uncertainties in the model-estimated spectral single-scattering albedos, see section 4.) Variations in the mineral composition of dust can have a profound impact on its optical properties (Sokolik and Toon 1999), which can be different between source regions. Thus, we limit our comparison only to those studies that treat Saharan dust. Quijano et al. (2000) used a high-level, explicit mineral optical model to compute the Saharan values, which they contrasted (not shown) to those computed for the Afghan region. Diaz et al. (2001) retrieved their value from surface-based, spectral sun photometer measurements taken from May to July. Haywood et al. (2001) used aircraft in situ nephelometer and particle soot absorption photometer measurements from two flights taken late April and early May. Kaufman et al. (2001) retrieved their value from Landsat satellite images from May and April. Also presented in Kaufman et al. (2001) are the National Aeronautics and Space Administration (NASA) Aerosol Robotic Network (AERONET) retrievals (Dubovik et al. 2000, 2002) from June to August.

(a)

(b)
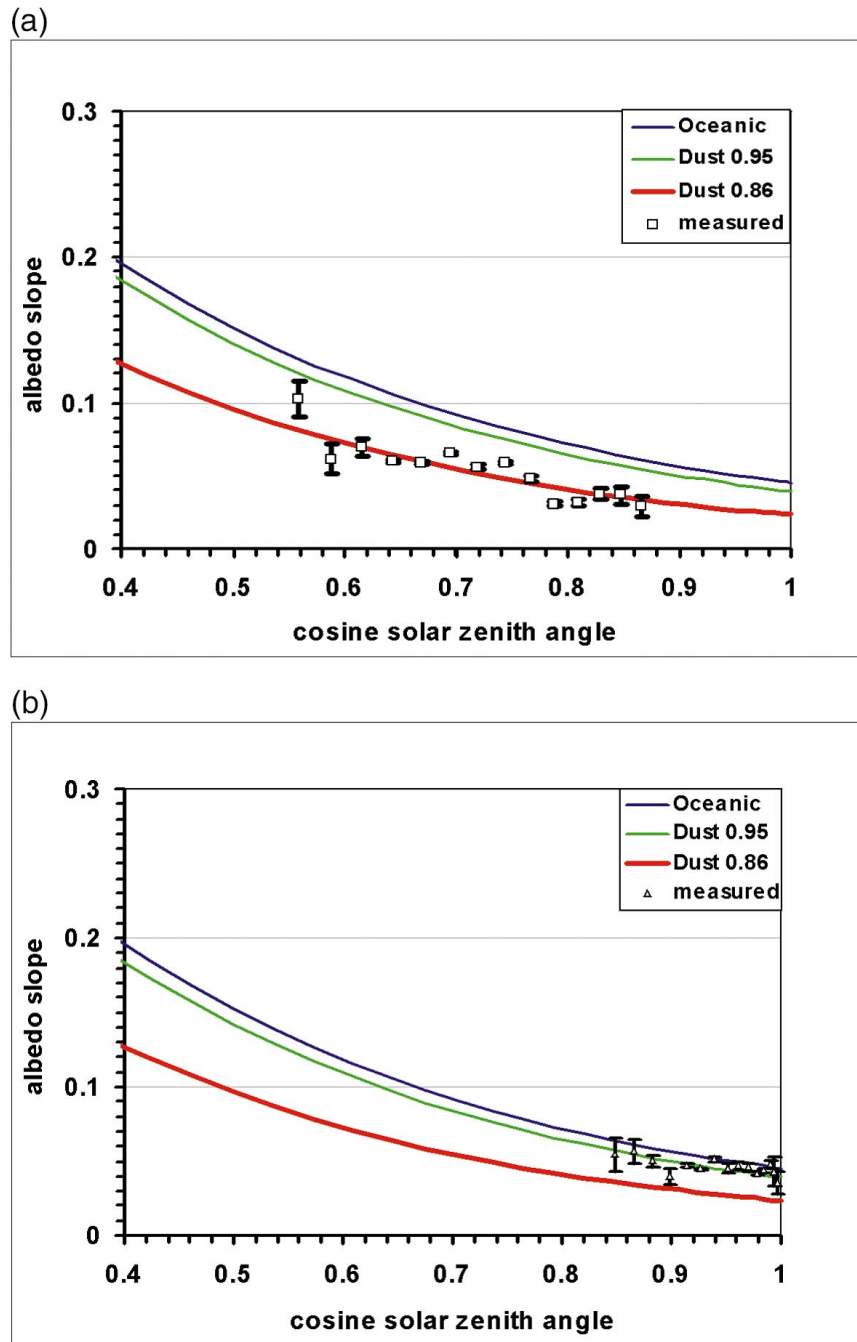
FIG. 7. Variation of the observed clear-sky albedo slopes, $d(\text{albedo})/d\tau_a$, with the cosine solar zenith angle (symbols) for (a) NDJ and (b) JJA. The albedo slopes are related to the aerosol forcing efficiency based on Eq. (3). The green and red curves show, respectively, the simulated albedo slopes using a single-scattering albedo (at 550 nm) of 0.95 and 0.86. The blue curve indicates the simulated result for the oceanic aerosol (conservative scattering).

Our JJA single-scattering albedo values (0.95 ± 0.04 at 550 nm) agree best with the less absorbing estimates by Kaufman et al. (2001) and the AERONET retrievals therein. For the NDJ period, our single-scattering albedo decreases to a value (0.86 ± 0.04 at 550 nm) that is more consistent with those reported by Quijano et al.

(2000), Diaz et al. (2001), and Haywood et al. (2001). Our spectral albedos for NDJ are similar to that by Diaz et al. (2001) and Haywood et al. (2001). Spectral dissimilarities could be related to differences in the dust size distribution, and the refractive index of the mineral compounds used. Past investigations suggest that dust
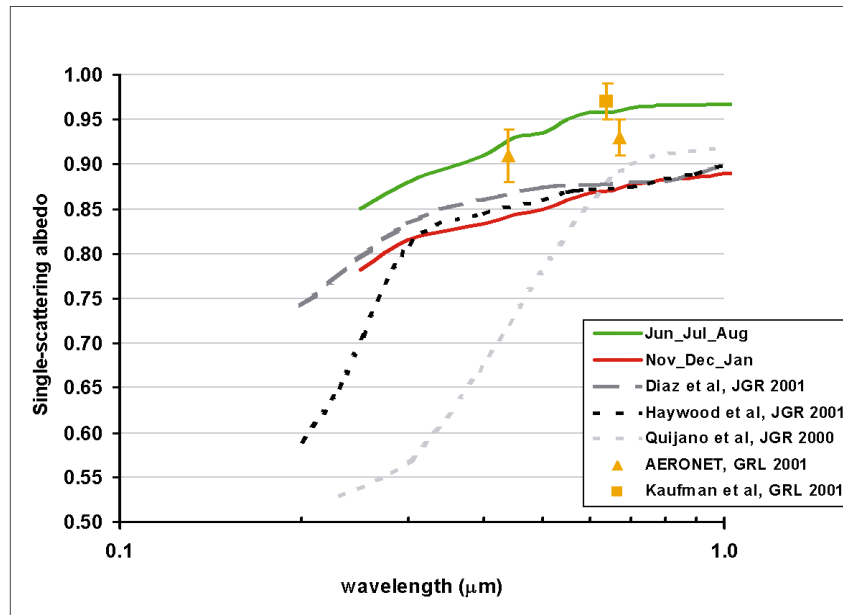
FIG. 8. Comparison of the wavelength dependence of the single-scattering albedos deduced
in this study to values for Saharan dust obtained from the literature.

single-scattering albedos lower than 0.9 (at 500 nm) would be associated with high amounts of hematite, an absorbing species (Sokolik and Toon 1996, 1999; Li et al. 1996). Further, Husar et al. (1997) and Diaz et al. (2001) suggested that this region might involve a mixture of dust and biomass-burning aerosols from equatorial Africa. This idea is supported by the MODIS Rapid Response System, which reveals a high frequency of fire spots in equatorial Africa during NDJ. Thus, the penetration of biomass-burning aerosols into the region might also contribute to these lower values.

Several studies have previously determined the aerosol forcing for Saharan dust for a study region similar to ours (Hsu et al. 2000; Quijano et al. 2000; Diaz et al. 2001; Haywood et al. 2001; Loeb and Kato 2002; Christopher and Zhang 2002). Unfortunately, we were not able to directly compare our forcing efficiencies to these other studies because of differences in the time of year studied, or in the type of forcing property reported. For example, the forcing properties reported for this region include instantaneous forcing, diurnal average forcing, and instantaneous forcing efficiency; but none of these other studies report diurnal average forcing efficiency. Forcing depends to first-order on the aerosol optical depth and, should the optical depth be different between studies (as they almost always are), a direct comparison is not possible. Instantaneous forcing values will also depend critically on the solar zenith angle. The diurnal average forcing efficiency, however, is by definition insensitive to the aerosol optical depth and is far less sensitive to solar geometry (although dramatically different solar geometries can have an effect). For these reasons, we recommend using diurnal average forcing

efficiency as the property that enables the most direct comparison of forcing values between studies.

4. Uncertainties

The methodology used to determine the diurnal forcing efficiencies boils down to three steps: 1) the $d(\text{albedo})/d\tau_a$ slopes per solar zenith angle bin are determined directly from the CERES and MODIS data; 2) an aerosol model is constructed, constrained to the MODIS effective radius, that matches the magnitude of the $d(\text{albedo})/d\tau_a$ slopes and their variation with solar zenith angle bin; 3) the model-generated curves, which provide the interpolation between the solar zenith angles and extrapolation beyond the angles that are directly accessible from the data, are integrated to yield the diurnal forcing efficiencies. The uncertainties and implicit assumptions within these steps are discussed in this section.

The $d(\text{albedo})/d\tau_a$ slopes are a principal parameter in the analysis and, as seen in Fig. 6, the current measuring and retrieving techniques produce scatter in the plots of the CERES TOA shortwave albedo and the MODIS AOD. This degree of scatter is somewhat typical and can be seen in similar studies. Two factors that may contribute to this scatter are the CERES ''ERBE-like'' scene identification, and the angular distribution models (ADMs) used for the radiance-to-flux conversion. Loeb and Kato (2002) estimate that the uncertainties in the average, direct radiative effects for the CERES ERBE-like product are about 3–5 W m^{-2} and are caused mainly by cloud contamination, the radiance-to-flux conversion, and instrument calibration. Further, the possible

presence of a soot–dust mixture during NDJ may further complicate selecting an appropriate ADM. While the scatter is evident in Fig. 6, we note that the slope method we used to determine the aerosol forcing efficiencies would remove the systematic bias that these factors may incur. The three fitting methods tested yield similar results, which suggest that the effects of the scatter are at least partly managed by the slope fitting, and the linear-direct method used is the least sensitive to scatter. Still, the combination of the scatter plus the reduced range of AOD for the low-dust months might lead to a greater uncertainty in the NDJ slope. Thus, the scatter and its effect on the slopes are considered to be the primary source of uncertainty for the forcing efficiency.

The effects of this uncertainty are felt by the analysis through the model d(albedo)$/d\tau_a$ (Fig. 7) that fit the observations and extrapolate beyond the solar zenith angles directly accessible. The constraints applied to the aerosol model fitting are stringent in that the simulated slopes must match the absolute magnitude (vertical offset in the curves), their variation with solar zenith angle, and match the MODIS-retrieved effective radius. The uncertainty in the observed slopes is translated into the uncertainty in the selection of the model used for fitting, which could affect the shape of the curve at the large solar zenith angles where observations are not available. It is for this reason that our uncertainty is determined from the rms between the fit and the observations that, in essence, provides an uncertainty "envelope" for the fitted curve.

While we are careful in constructing our aerosol models, it is possible that a slightly different combination of aerosol parameters could also produce a close fit to the observations, but whose angular behavior may be different at large solar zenith angles. In addition, other model uncertainties might affect the smoothly varying angular behavior, such as the aerosol height profile. While the profile used is representative of that commonly found in the atmosphere, an upward or downward shift in the profile could perturb the aerosol scattering properties slightly from those that matched the observations. Such differences would be magnified at higher solar zenith angles (because of the longer optical path); however, their total effect on the forcing efficiency would be moderated by the corresponding cosine decrease in incident solar radiation. Thus, a dominant factor affecting the forcing efficiencies is the observed points near low (overhead) solar zenith angles. The pronounced vertical offset between the JJA and NDJ observations signifies a clear difference in the aerosol character between the seasons. Even if such uncertainties are manifested and produced a bias, the relative seasonal differences should stand.

Implicit within the fitting of the broadband slopes is the spectral variation of the model aerosol properties. Within each season, it stands to reason that, to first order, the aerosol flow from the strong source regions should produce a similar aerosol character for the period. As noted before, aerosol spectral properties tend, in general, to be broad and smoothly varying (especially for large dust particles). Our fitting procedure is likely most sensitive to the aerosol properties in the vicinity of 550 nm because of the large amount of shortwave energy incident at (or near) this wavelength, and the corresponding effect of this energy on the broadband CERES flux. The degree of aerosol spectral variation allowed in the model is constrained by using the MODIS-retrieved effective radius. As seen in Fig. 8, the estimated spectral variations in the single-scattering albedo for our two seasons both show a similar gradual change with wavelength (not an abrupt structure), and this general pattern is supported by two other studies shown. In addition to the single-scattering albedo uncertainty provided at 550 nm (which may be an upper limit), we estimate that the spectral uncertainty may increase at wavelengths significantly far from the energetic 550-nm region.

Current MODIS retrievals assume that aerosols are spherical (S. Mattoo 2002, personal communication), but dust is nonspherical and the associated differences in the scattering properties may cause biases in the retrievals of dust properties. Tanre et al. (2001) found that dust nonspherical effects on its optical properties are not significant for the scattering angles less than 120°. However, Mishchenko et al. (2000) determined that there can be a factor of 2 difference between the ratios of the phase functions for spherical and nonspherical particles at a scattering angle of 120°. Figure 9 shows that many of the MODIS scattering angles for our study region are greater than 120°. Specifically, for sample days in November and July, the pixels with scattering angles greater than 120° are, respectively, 67% and 82% (Fig. 9c). Results from the Puerto Rico Dust Experiment (PRIDE) quantify errors in the MODIS retrievals of dust properties, which may be caused by untreated nonspherical effects (Levy et al. 2003). MODIS retrievals of AOD at 0.66 μm agreed well with sun photometer measurements, but produced retrievals that were too large at 0.47 and 0.55 μm and too small at 0.87 μm. This results in MODIS particle size retrievals that are too small compared to the in situ measurements (Levy et al. 2003). This may explain why the effective radii shown in Fig. 5 for JJA are much smaller than the 1.5–2.5-μm value used by Kaufman et al. (2001). Even so, the relative differences in the MODIS radii between the JJA and NDJ in Fig. 5 are likely representative, albeit shifted towards smaller sizes compared to truth. We note that the MODIS retrievals of flux, AOD, and effective radius are based on the spherical theory, and that the SBDART simulations use OPAC parameters that are also based on spherical theory. Thus, spherical theory is used to obtain the observed d(albedo)$/d\tau_a$ as well as the model-generated d(albedo)$/d\tau_a$ to which the observations are compared. By being internally consistent with the use of spherical theory, the modeling should provide a solution that is radiatively consistent with the MODIS parameters and, thereby, we minimize the po-
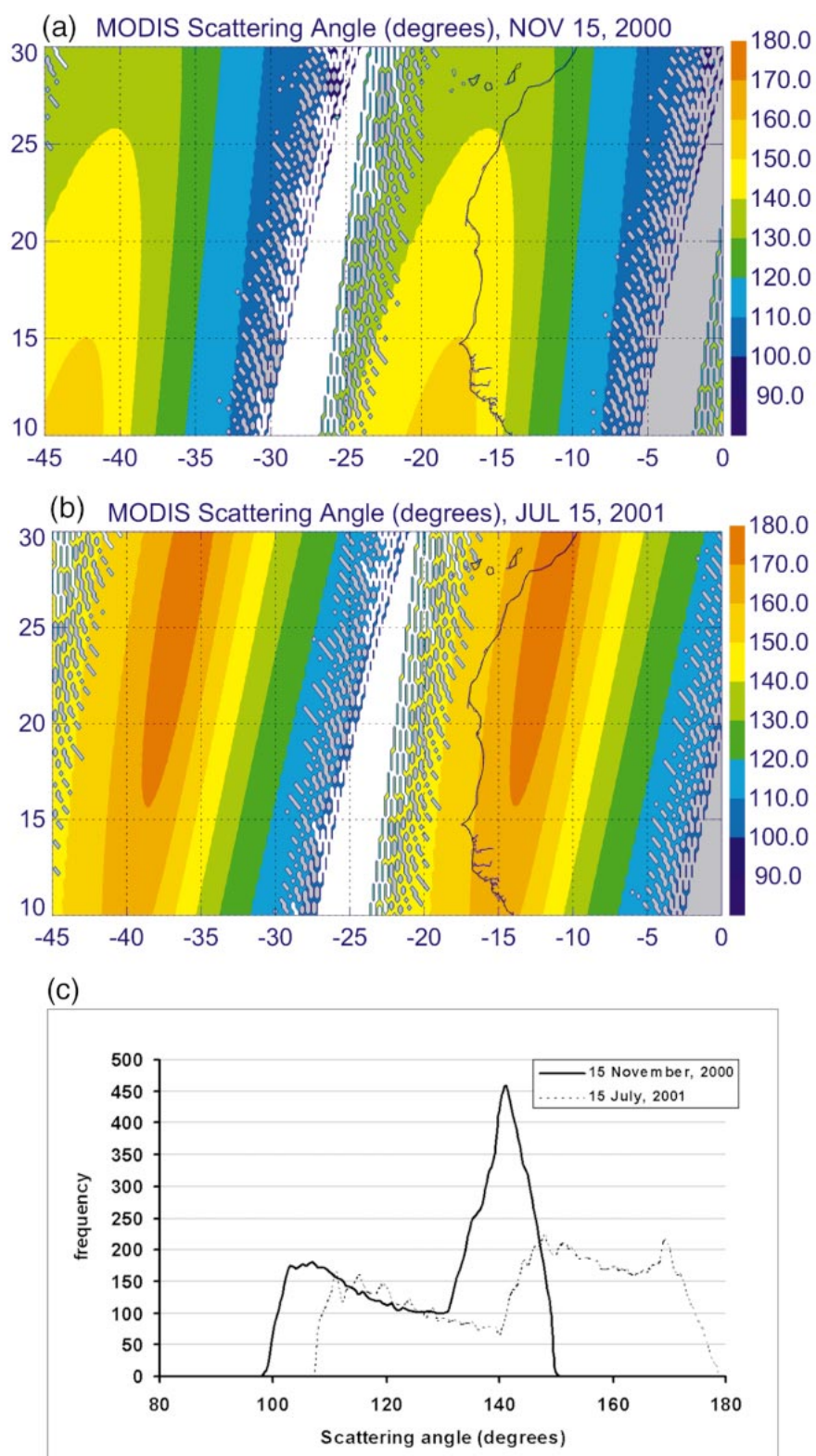
FIG. 9. Distribution of the MODIS scattering angle (Θ) on (a) 15 Nov 2000 and (b) 15 Jul 2001. (c) Their frequency distributions. Many pixels have a scattering angle greater than 120°, for which dust nonspherical influences on the retrievals may be important.

tential impact that nonspherical effects could have on the interpretation of our slopes and forcing efficiencies.

5. Conclusions

This study examines the dust aerosol radiative forcing over a study region off the northern coast of the Sahara. A change in the aerosol forcing efficiency (which is normalized by the magnitude of the aerosol optical depth) indicates a change to the radiative character of the aerosol (e.g., size and/or composition). The top-of-atmosphere (TOA) diurnal mean forcing efficiency is -35 ± 3 W m^{-2} τ_a^{-1} for the high-dust season (June–August), and -26 ± 3 W m^{-2} τ_a^{-1} during the low-dust season (November–January). The difference in these efficiencies correspond to reducing the aerosol single-scattering albedo from 0.95 during the dusty season to about 0.86 for the low-dust season, and are accompanied by a reduction in the aerosol effective radius. These changes might be caused by the invasion of biomass-burning aerosols from equatorial Africa.

The larger aerosol absorption affects not only the energy balance at the TOA, but also at the surface. Based on model extrapolations, the absolute value of the surface forcing efficiencies may increase from -65 W m^{-2} τ_a^{-1} for the high-dust season to -81 W m^{-2} τ_a^{-1} for the low-dust season. The ratios of the surface-to-TOA efficiencies are, respectively, 1.8 and 3.1, which demonstrate a dramatic difference (72%) in how the solar energy is partitioned between the TOA and surface for these two cases. However, it is interesting to note that the surface forcing for the two seasons could be similar, since the difference in seasonal surface forcing efficiencies would be partially compensated by the opposing differences in magnitudes of the seasonal average AODs.

Our values of the dust single-scattering albedo during the high-dust period (JJA) are consistent with the less absorbing value suggested by Kaufman et al. (2001). However, our lower value during the low-dust season corresponds to the values suggested by Quijano et al. (2000), Diaz et al. (2001), and Haywood et al. (2001). Thus, our results indicate the complexities involved in prescribing the aerosol properties within a region. These results show that the aerosol radiative character within a region can be readily modified, even immediately adjacent to a powerful source region such as the Sahara. This study provides important observational constraints for models of dust radiative forcing.

Finally, we note that there are many different types of properties used to quantify aerosol forcing, which include instantaneous forcing, diurnal average forcing, and instantaneous forcing efficiency. However, intercomparing these forcing properties between studies is impossible unless the aerosol optical depth and/or solar geometry are the same, which they rarely are. To facilitate comparisons between studies, we recommended that studies express the aerosol radiative effect in terms of diurnal average aerosol forcing efficiency, which is least sensitive to factors such as aerosol optical depth and solar geometry.

REFERENCES

Andreae, M. O., 1995: Climatic effects of changing atmospheric aerosols level. *Future Climates of the World,* Vol. 16, A. Henderson-Sellers, Ed., World Survey of Climatology, Elsevier, 341–392.

Christopher, S. A., and J. Zhang, 2002: Shortwave aerosol radiative forcing from MODIS and CERES observations over the oceans. *Geophys. Res. Lett.,* **29,** 1859, doi:10.1029/2002GL014803.

Conant, W. C., 2000: An observational approach for determining aerosol surface radiative forcing: Results from the first field phase of INDOEX. *J. Geophys. Res.,* **105,** 15 347–15 360.

d'Almeida, G. A., P. Koepke, and E. P. Shettle, 1991: *Atmospheric Aerosols: Global Climatology and Radiative Characteristics.* A. Deepak Publishing, 561 pp.

Diaz, J. P., F. J. Exposito, C. J. Torres, F. Herrera, J. M. Prospero, and M. C. Romero, 2001: Radiative properties of aerosols in Saharan dust outbreaks using ground-based and satellite data: Applications to radiative forcing. *J. Geophys. Res.,* **106,** 18 403–18 416.

Dubovik, O., A. Smirnov, B. N. Holben, M. D. King, Y. J. Kaufman, T. F. Eck, and I. Slutsker, 2000: Accuracy assessment of aerosol optical properties retrieval from AERONET sun and sky radiation measurements. *J. Geophys. Res.,* **105,** 9791–9806.

——, B. N. Holben, T. F. Eck, A. Smirnov, Y. J. Kaufman, M. D. King, D. Tanre, and I. Slutsker, 2002: Variability of absorption and optical properties of key aerosol types observed in worldwide locations. *J. Atmos. Sci.,* **59,** 590–608.

Duce, R., 1995: Sources, distributions, and fluxes of mineral aerosols and their relationship to climate. *Aerosol Forcing of Climate,* R. J. Charlson and J. Heintzonborg, Eds., Wiley, 43–72.

Ellis, W. G., Jr., and J. T. Merrill, 1995: Trajectories for Saharan dust transport to Barbados using Stokes's law to describe gravitational settling. *J. Appl. Meteor.,* **34,** 1716–1726.

Fouquart, Y., B. Bonnel, G. Brogniez, J. C. Buriez, L. Smith, J.-J. Morcrette, and A. Cerf, 1987: Observations of Saharan aerosols: Results of ECLATS field experiment. Part II: Broadband radiative characteristics of the aerosols and vertical radiative flux divergence. *J. Climate Appl. Meteor.,* **26,** 38–52.

Haywood, J. M., P. N. Francis, M. D. Glew, and J. P. Taylor, 2001: Optical properties and direct radiative effect of Sharan dust: A case study of two Saharan dust outbreaks using aircraft data. *J. Geophys. Res.,* **106,** 18 417–18 430.

Hess, M., P. Koepke, and I. Schult, 1998: Optical properties of aerosols and clouds: The software package OPAC. *Bull. Amer. Meteor. Soc.,* **79,** 831–844.

Hignett, P., J. P. Taylor, and P. N. Francis, 1999: Comparison of observed and modeled direct aerosol forcing during TARFOX. *J. Geophys. Res.,* **104,** 2279–2287.

Hsu, N. C., J. R. Herman, and C. Weaver, 2000: Determination of radiative forcing of Saharan dust using combined TOMS and ERBE data. *J. Geophys. Res.,* **105,** 20 649–20 661.

Husar, R. B., J. M. Prospero, and L. L. Stowe, 1997: Characteriza-

tion of tropospheric aerosols over the ocean with the NOAA AVHRR optical thickness operational product. *J. Geophys. Res.,* **102,** 16 889–16 909.

Kaufman, Y. J., A. Karnieli, and D. Tanré, 2000: Detection of dust over the desert by EOS-MODIS. *IEEE Trans. Geosci. Remote Sens.,* **38,** 525–531.

——, D. Tanre, O. Dubovik, A. Karnieli, and L. A. Remer, 2001: Absorption of sunlight by dust as inferred from satellite and ground-based remote sensing. *Geophys. Res. Lett.,* **28,** 1479–1482.

Koepke, P., M. Hess, I. Schult, and E. P. Shettle, 1997: Global aerosol data set. MPI Meteorologie Hamburg Rep. 243, 44 pp.

Levy, R. C., and Coauthors, 2003: Evaluation of the Moderate-Resolution Imaging Spectroradiometer (MODIS) retrievals of dust aerosol over the ocean during PRIDE. *J. Geophys. Res.,* **108,** 8594, doi:10.1029/2002JD002460.

Li, F., and V. Ramanathan, 2002: Winter to summer monsoon variation of aerosol optical depth over the tropical Indian Ocean. *J. Geophys. Res.,* **107,** 4284, doi:10.1029/2001JD000949.

Li, X., H. Maring, D. Savoie, K. Voss, and J. M. Prospero, 1996: Dominance of mineral dust in the aerosol light-scattering in the North Atlantic trade winds. *Nature,* **380,** 416–419.

Loeb, N. G., and S. Kato, 2002: Top-of-atmosphere direct radiative effect of aerosols over the tropical ocean from the Clouds and the Earth's Radiant Energy System (CERES) satellite instrument. *J. Climate,* **15,** 1474–1484.

Mbourou, G. N., J. J. Bertrand, and S. E. Nicholson, 1997: The diurnal and seasonal cycles of wind-borne dust over Africa north of the equator. *J. Appl. Meteor.,* **36,** 868–882.

Mishchenko, M. I., J. W. Hovenier, and L. D. Travis, 2000: *Light Scattering by Nonspherical Particles: Theory, Measurements, and Applications.* Academic Press, 690 pp.

Quijano, A., I. Sokolik, and O. B. Toon, 2000: Radiative heating rates and direct radiative forcing by mineral dust in cloudy atmospheric conditions. *J. Geophys. Res.,* **105,** 12 207–12 219.

Rajeev, K., and V. Ramanathan, 2001: Direct observations of clear-sky aerosol radiative forcing from space during the Indian Ocean experiment. *J. Geophys. Res.,* **106,** 17 221–17 235.

Ricchiazzi, P., S. Yang, C. Gautier, and D. Sowle, 1998: SBDART: A research and teaching software tool for plane-parallel radiative transfer in the earth's atmospheres. *Bull. Amer. Meteor. Soc.,* **79,** 2101–2114.

Satheesh, S. K., and V. Ramanathan, 2000: Large differences in tropical aerosol forcing at the top of the atmosphere and earth's surface. *Nature,* **450,** 60–63.

Shettle, E. P., and R. W. Fenn, 1979: Models for the aerosols of the lower atmosphere and the effects of humidity variations on their optical properties. AFGL-TR-79-0214, 94 pp. [Available from AFCRL, Hanscom Field, Bedford, MA 01731.]

Sokolik, I. N., and O. B. Toon, 1996: Direct radiative forcing by anthropogenic airborne mineral aerosols. *Nature,* **381,** 681–683.

——, and ——, 1999: Incorporation of mineralogical composition into models of the radiative properties of mineral aerosol from UV to IR wavelengths. *J. Geophys. Res.,* **104,** 9423–9444.

Tanre, D., and Coauthors, 2001: Climatology of dust aerosol size distribution and optical properties derived from remotely sensed data in the solar spectrum. *J. Geophys. Res.,* **106,** 18 205–18 217.

Weaver, C. J., P. Ginoux, N. C. Hsu, M. D. Chou, and J. Joiner, 2002: Radiative forcing of Saharan dust: GOCART model simulations compared with ERBE data. *J. Atmos. Sci.,* **59,** 736–747.

Wielicki, B. A., B. R. Barkstrom, E. F. Harrison, R. B. Lee III, G. L. Smith, and J. E. Cooper, 1996: Clouds and the Earth's Radiant Energy System (CERES): An earth observing system experiment. *Bull. Amer. Meteor. Soc.,* **77,** 853–868.